# Journal Pre-proof

Insights for optimum cation defects in photocatalysis: a case study of hematite nanostructures

Sheng-qi Guo, Zhenzhong Hu, Mengmeng Zhen, Bingchuan Gu, Boxiong Shen, Fan Dong

PII: S0926-3373(19)31252-4

DOI: https://doi.org/10.1016/j.apcatb.2019.118506

Reference: APCATB 118506

To appear in: Applied Catalysis B: Environmental

Received Date: 26 June 2019

Revised Date: 4 November 2019

Accepted Date: 1 December 2019

Please cite this article as: Sheng—qi G, Zhenzhong H, Mengmeng Z, Bingchuan G, Boxiong S, Fan D, Insights for optimum cation defects in photocatalysis: a case study of hematite nanostructures, *Applied Catalysis B: Environmental* (2019), doi: https://doi.org/10.1016/j.apcatb.2019.118506

This is a PDF file of an article that has undergone enhancements after acceptance, such as the addition of a cover page and metadata, and formatting for readability, but it is not yet the definitive version of record. This version will undergo additional copyediting, typesetting and review before it is published in its final form, but we are providing this version to give early visibility of the article. Please note that, during the production process, errors may be discovered which could affect the content, and all legal disclaimers that apply to the journal pertain.

© 2019 Published by Elsevier.



Insights for optimum cation defects in photocatalysis: a case study of hematite

nanostructures

Sheng-qi Guo<sup>a</sup>, Zhenzhong Hu<sup>a</sup>, Mengmeng Zhen<sup>a</sup>, Bingchuan Gu<sup>c</sup>, Boxiong

Shen<sup>a,\*</sup>, Fan Dong<sup>b</sup>

<sup>a</sup> Tianjin Key Laboratory of Clean Energy and Pollution Control, School of Energy and

Environmental Engineering, Hebei University of Technology, Tianjin 300401, P. R. China

<sup>b</sup> Institute of Fundamental and Frontier Sciences, University of Electronic Science and Technology

of China, Chengdu 611731, China

<sup>c</sup> State Key Laboratory of Particle Detection and Electronics, University of Science & Technology

of China, Hefei, Anhui 230026, China

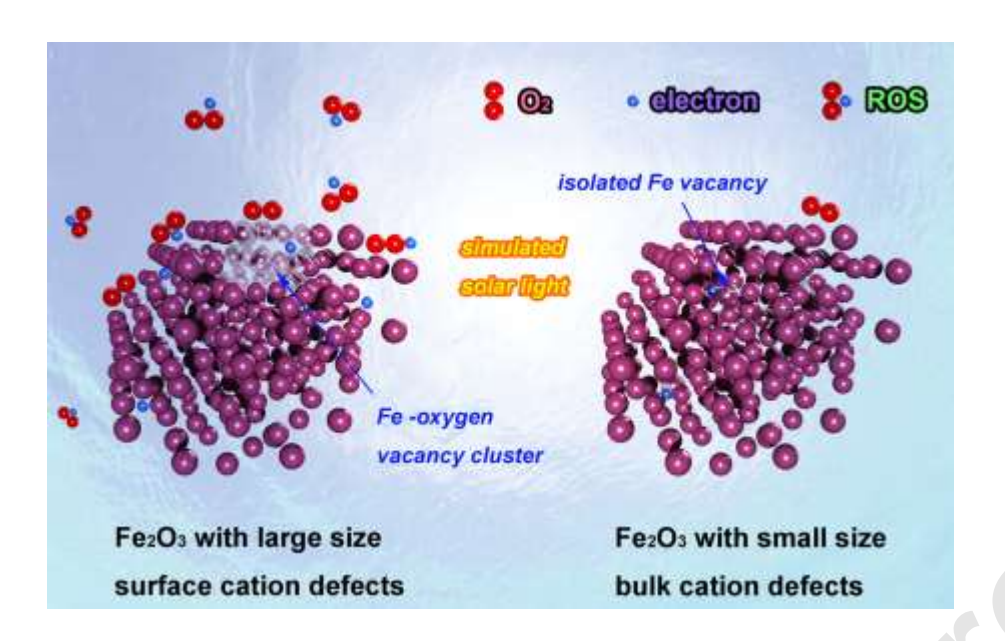
Keywords: Cation defect, α-Fe<sub>2</sub>O<sub>3</sub>, Photocatalysis, Density functional theory computation,

Reaction mechanism

Corresponding author:

E-mail address: shenbx@hebut.edu.cn

Graphical abstract



### High lights

- A series of α–Fe<sub>2</sub>O<sub>3</sub> nanostructures with tunable cation defects were synthesized.
- Theoretical calculations and experiments identify different types of cation defects.
- The photocatalytic degradation activity of BPA by different materials was studied.
- Uncovering the role of cation defects in affecting photocatalytic activity.

#### **ABSTRACT**

The effect of defects on photoinduced electron-hole (e-h) separation is remaining unclear; especially the role of cation defects is poorly understood. In this work, a series of  $\alpha$ -Fe<sub>2</sub>O<sub>3</sub> nanostructures with tunable cation defects were synthesized and characterized with positron annihilation. We discover that increasing the relative concentration ratio of large size surface cation defects (LSCD) to smaller size bulk cation defects (SBCD) in  $\alpha$ -Fe<sub>2</sub>O<sub>3</sub> facilitates the improvement of separation efficiency for photogenerated e-h pairs. Both theory and experiment data demonstrate that when the relative concentration ratio of LSCD to SBCD increases, oxygen

molecules are more likely adsorbed on the surface of the  $\alpha$ –Fe<sub>2</sub>O<sub>3</sub> nanostructure and are prone to transfer electron, thereby forming more reactive oxygen species (ROS). This work provides insight into finding the optimum cation defect that contributes to the photocatalytic process, and provides a new idea for designing high efficiency photocatalysts based on defect engineering.

#### 1. Introduction

Photocatalysts can enhance many applications in diverse fields, such as energy conversion and water/wastewater treatment [1-3]. One of the most important factors determining the efficiency and practical applicability of semiconductor photocatalysts is the ability to effectively generate photo-induced electron-hole (e-h) pairs and prevent their recombination [4-6]. During the past decades, various strategies have been developed for the enhancement of e-h separation, such as doping, semiconductor recombination, and controlling exposed crystal facet, *etc* [7-12].

Recent studies show that defect engineering is expected to be another powerful means of improving the e-h separation efficiency of semiconductor [13-15]. Through defect engineering, the electronic structures of semiconductor can be significantly changed even at defect concentrations as low as one defect per one hundred million host atoms [16,17]. More importantly, many studies have proved that defects can increase the e-h separation efficiency, in which the defects can serve as the adsorption sites for effectively limiting photoexcited electrons transfer and hence prevent their recombination with the photogenerated holes [18-22]. However, some other studies presented diametrically opposite results that defects would act as a recombination center for e-h pairs, hindering the progress of the catalytic reaction [23,24]. Indeed, these contradictory effects of defects are primarily derived from the diversity of defect types and the complexity of the structural environment in which they are located. In other words, the evaluation of the influence mechanism of different types of defects on photocatalytic performance is still in its infancy.

Although defect engineering has been considered as a promising direction for developing highly active photocatalysts, our knowledge of defect—dependent photocatalytic performance is mostly limited to anion defect, such as oxygen vacancy defect [25-28]. In comparison, the roles of cation defect in photocatalysis are usually ignored. In fact, cation defect closely affects the conductivity of the material, which is a key factor in determining the charge carrier separation rate [29]. To date, only very few studies investigated the cation defect—dependent performance of photocatalytic [30]. Yet, no prior research has been reported on the determination and mechanism study of the type of optimum cation defects, which is of great significance for assessing the importance of cationic defects to photocatalytic activity and understanding the contribution of cation defects.

In this work, a series of hematite ( $\alpha$ –Fe<sub>2</sub>O<sub>3</sub>) nanostructures with tunable cation defects were synthesized and characterized with positron annihilation. We observe that the  $\alpha$ –Fe<sub>2</sub>O<sub>3</sub> nanorods with a higher relative concentration ratio of large size cation defects (Fe<sup>3+</sup>–oxygen vacancy clusters) to smaller size cation defects (isolated Fe vacancy) exhibit a higher photocatalytic activity in the degradation of bisphenol A (BPA) under visible light than the  $\alpha$ –Fe<sub>2</sub>O<sub>3</sub> nanocubes with a lower relative concentration ratio of large size cation defects to smaller size cation defects. Based on the density functional theory computations and zeta–potential analysis, we corroborate that the small size defects mainly exist in the bulk of the  $\alpha$ –Fe<sub>2</sub>O<sub>3</sub>, while the larger size defects mainly locate on the surface of the  $\alpha$ –Fe<sub>2</sub>O<sub>3</sub>. These surface defects facilitate photoexcitation of electrons and reduce the O<sub>2</sub> adsorption energy on material surface, which significantly promotes the reactive oxygen species (ROS) generating, enhancing photocatalytic activity of materials.

### 2. Experimental

### 2.1. Materials and fabrication

All reagents involved in this work were of analytical grade and were used as received without

further purification. The  $\alpha$ –Fe<sub>2</sub>O<sub>3</sub> nanorods with a higher relative concentration ratio of large size surface cation defects (LSCD) to smaller size bulk cation defects (SBCD) were synthesized by a facile hydrothermal process. In a typical synthesis procedure, 2.0 mmol (800 mg) Fe<sub>2</sub>(SO<sub>4</sub>)<sub>3</sub>, 12.0 mmol (480 mg) NaOH, 2.0 mmol (700 mg) sodium dodecyl benzene sulfonate (SDS) and different amount of 2, 2'–bipyridine (2, 2'–bpy, 20 mg, 50 mg, 80 mg and 110 mg) were dissolved in 30 mL water by vigorously stirring for 10 min. Then, the mixture was sealed in a 50–mL Teflon–lined stainless–steel autoclave and heated at 150 °C for 24 h. After the mixture cooled to room temperature, the resulting precipitates were washed with deionized water and absolute ethanol, and then dried at 60 °C for 12 h. Finally, the reddish-brown product was obtained, labeled as Fe<sub>2</sub>O<sub>3</sub>–S–X (where X represents the amount of 2, 2'–bpy).

The  $\alpha$ -Fe<sub>2</sub>O<sub>3</sub> nanocubes with a lower relative concentration ratio of LSCD to SBCD were prepared by the same procedure as Fe<sub>2</sub>O<sub>3</sub>-S-X except without 2, 2'-bpy, which is denoted as Fe<sub>2</sub>O<sub>3</sub>-B.

### 2.2. Characterization

Samples morphology was determined by scanning electron microscopy (SEM, Nova Nano SEM 460, FEI) and transmission electron microscopy (TEM, Talos F200X, FEI). The X-ray diffraction (XRD) patterns (Rigaka D/max2500) with Cu Ka radiation (λ = 1.54056 Å) were used to confirm the phase of the samples. The element composition of the samples was analysed by X-ray photoelectron spectroscopy (XPS, ESCALAB250Xi). UV-visible spectrophotometer (Lambda 750 UV/VIS/NIR) was used for characterizing the band gap structure of the samples. The surface functional group information of the samples was obtained by FT–IR spectra (Frontier Mid-IR FTIR). The Brunauer-Emmett-Teller (BET) specific surface area and pore structure of the samples was analyzed by nitrogen adsorption using a nitrogen adsorption apparatus (Autosorb-iQ-MP).

The zeta-potentials measurements were carried out by the Nano–ZS zetasizer (Malvern Instruments). Oxygen vacancy defect concentration and ROS determination by room–temperature electron spin resonance (ESR) spectra (EMXplus-6/1) at 300 K and 9.062 GHz. Steady-state photoluminescence (PL) spectra were obtained on a luminescence spectrometer (Jobin Yvon Fluorolog 3-TAU). The surface photovoltage (SPV) data was done using surface photovoltage spectrometer (CEL-SPS1000). Fluorescence lifetime results were obtained by transient fluorescence spectroscopy (FLSP920 Multifunction Steady State and Transient State Fluorescence Spectrometer).

Electrochemical impedance spectroscopy (EIS) was executed at 0.0 V, using an impedance measurement workstation unit in the frequency range of 0.1–10<sup>6</sup> Hz with a sinusoidal AC perturbation of 5 mV. Approximately 100 mg of Fe<sub>2</sub>O<sub>3</sub> powder sample was mixed with 0.5 mL of alpha-terpineol and stirred for 30 min. Then, a film was made using doctor–blade method on fluorine–doped tin oxide (FTO) conductive glass and obtained the counter electrode (CE). EIS was executed on dummy cells with a typical symmetric sandwich–like structure (i.e., CE/electrolyte/CE) with visible light irradiation.

### 2.3. Positron annihilation measurements

The positron lifetime experiments were carried out using a fast–fast coincidence ORTEC system (Oak Ridge Technology & Engineering Cooperation) with a time resolution of ~240 ps full width at half–maximum. A 30  $\mu$ Ci source of Na was sandwiched between two identical samples, and the total count was 1 million. Positron lifetime calculations were carried out using the ATSUP method [31], in which the electron density and the positron crystalline Coulomb potential were constructed by the non–self–consistent superposition of free atom electron density and Coulomb potential in the absence of the positron. We used  $3\times3\times3$  supercells for positron lifetime calculations of

unrelaxed structure mono-vacancy defects and vacancy associated in α-Fe<sub>2</sub>O<sub>3</sub>. To obtain the electron density and the Coulomb potential due to the nuclei and the electron density, several self-consistent calculations for electronic structures were performed with the fit-QMCGGA (QMC: quantum Monte Carlo; GGA: generalized gradient approximation) approach or electron-electron exchange correlations. To obtain the positron lifetimes, the GGA form of the enhancement factor proposed by Barbiellini was chosen [32].

### 2.4. Computational details

First-principles calculations were performed using pseudopotential based upon the density functional theory (DFT) as implemented in the VASP code [33]. These computations utilized Perdew-Burke-Ernzerhof (PBE) in the general gradient approximation (GGA) to describe the exchange-correlation interaction [34]. A cutoff energy of 500 eV was employed for all computations and  $3\times3\times1$  Monkhorst-Pack k-mesh was generated for the systems. A vacuum layer of 15 Å was used to avoid the spurious interactions between adjacent surfaces. The convergence threshold for structural optimization was set to be 0.02 eV/Å in force and  $10^{-5} \text{ eV}$  in energy. The adsorption energy of oxygen molecule adsorbed on the substrate was calculated by the following equation:

$$E_{
m ads} = E_{
m tot} - E_{
m substrate} - E_{
m oxygen\ molecule}$$

Where the  $E_{\text{total}}$  and  $E_{\text{substrate}}$  are the total energies of the relaxed  $\alpha$ –Fe<sub>2</sub>O<sub>3</sub> model with and without oxygen molecule, respectively; the  $E_{\text{oxygen molecule}}$  is the calculated energy of one oxygen molecule.

Partial atomic charges were obtained using Bader charge analysis as implemented by Henkelman and co-workers [35].

### 2.5. Photocatalytic experiments

The photocatalytic activity of the samples was evaluated by photocatalytic degradation of

bisphenol A (BPA), using an XPA system photochemical reactor (Nanjing Xujiang Electromechanical Plant). Photocatalytic experiments were carried out at room temperature, using a 500 W Xe lamp as visible light source device (light intensity was ~7 mW cm<sup>-2</sup>). In the specific photocatalytic degradation process, 0.31 mmol (50 mg) of  $\alpha$ –Fe<sub>2</sub>O<sub>3</sub> sample was dispersed in 50 mL of BPA aqueous solution (1×10<sup>-5</sup> M). Subsequently, the reaction started, and 5 mL of the suspension was withdrawn every 1 h and centrifuged to remove the catalyst. The concentration of BPA was analyzed using UV–vis spectroscopy (characteristic absorption peak of BPA at  $\lambda$  = 275 nm).

Photocatlytic degradation of BPA intermediates was determined by a liquid chromatography (LC)/mass spectrum (MS)/MS system (Waters Xevo TQ-S).

#### 3. Results and discussion

#### 3.1. Phase and microstructure

The samples of α-Fe<sub>2</sub>O<sub>3</sub> with higher relative concentration ratio of large size surface cation defects (LSCD) to smaller size bulk cation defects (SBCD) were prepared via a facile hydrothermal process at 150 °C (denoted as Fe<sub>2</sub>O<sub>3</sub>–S–X, X = 20, 50, 80, 110). Another sample of  $\alpha$ –Fe<sub>2</sub>O<sub>3</sub> with a lower relative concentration ratio of LSCD to SBCD was prepared by the same procedure except without 2, 2'-bpy (denoted as Fe<sub>2</sub>O<sub>3</sub>-B). The XRD patterns of the as-prepared samples (Fig. 1a) can be indexed as hexagonal  $\alpha$ -Fe<sub>2</sub>O<sub>3</sub> (JCPDS No. 33–0664) in the space group R-3c, with the lattice parameters of a = b = 0.504 nm and c = 1.375 nm, and no other impurities can be detected. The detailed chemical composition of the samples was investigated by the XPS analysis. XPS survey spectra (Fig. 1b) show that Fe, O and C elements coexist in the samples, indicating that the all nanostructures are pure (where the C element comes from the adventitious carbon from the XPS instrument). As can be seen from Fig. 1c and 1d, the Fe 2p peak splits into Fe 2p<sub>3/2</sub> at 709.7 eV and Fe 2p<sub>1/2</sub> at 724.4 eV, and the peak at 529.7 eV can correspond to the O 1s peak, which is in agreement with reported data on α–Fe<sub>2</sub>O<sub>3</sub> [36]. The characteristics and positions of Fe 2p and O 1s peaks were consistent in the different samples, meaning that the introduction of 2, 2'-bpy did not change the lattice structure of α-Fe<sub>2</sub>O<sub>3</sub>. In addition, the Fe/O atom ratio in all Fe<sub>2</sub>O<sub>3</sub>-S-X samples is observed smaller than that of Fe<sub>2</sub>O<sub>3</sub>–B (Table S1), which indicates that the introduction of 2, 2'-bpy to synthesis system leads to an increase in cation defects. The FT-IR spectrum show the absence of organic matter on the surfaces of both Fe<sub>2</sub>O<sub>3</sub>-B and Fe<sub>2</sub>O<sub>3</sub>-S-X (Fig. S1). It can be observed that there are broad peaks at 3430, 1615 and 1395 cm<sup>-1</sup> for the all samples, which correspond to the surface adsorbed water and hydroxyl groups, implying the final products are clean. In addition, we found that the curve shape in FT-IR specta show almost no difference

between Fe<sub>2</sub>O<sub>3</sub>–S–X and Fe<sub>2</sub>O<sub>3</sub>–B, meaning that changing in the synthesis conditions do not cause changes in Fe<sub>2</sub>O<sub>3</sub>–S–X structure network, which still remain the same as Fe<sub>2</sub>O<sub>3</sub>–B.

Fig. 2, S2 and S3 show typical microstructures of the samples. The panoramic views (Fig. 2a, S3a-S3c) reveal that the Fe<sub>2</sub>O<sub>3</sub>-S-X samples consist entirely of nanorod architectures without impurity particles or aggregates. Typical TEM images (Fig. 2b, S3d-S3f) show that the length of the randomly selected nanorods of Fe<sub>2</sub>O<sub>3</sub>-S-X is 100-300 nm. Different from the Fe<sub>2</sub>O<sub>3</sub>-S-X, the Fe<sub>2</sub>O<sub>3</sub>-B exhibits uniform nanocubes morphology with average diameter of 80 nm (Fig. S2a and S2b), which indicates that the introduction of 2, 2' -bpy not only affect the defect characteristics, but also lead to morphology change of the products. High resolution transmission electron microscopy (HR-TEM) analysis (Fig. 2c, S2c and S3g-S3i) exhibit clear lattice fringes with a dihedral angle of 86° and the interplanar distance is calculated to be 0.36 nm, indicating that all samples are dominantly exposed {012} facets. Excellent crystallinity of the samples is confirmed from the corresponding selected—area electron diffraction (SAED) pattern (Fig. 2d, S2d and S3j-S3l), which clearly exhibits the single-crystal nature of both Fe<sub>2</sub>O<sub>3</sub>-S-X and Fe<sub>2</sub>O<sub>3</sub>-B sampels. The spots can be indexed to (012) and (112) of hexagonal α-Fe<sub>2</sub>O<sub>3</sub>, respectively. Moreover, the N<sub>2</sub> adsorption/desorption isotherms of the samples show the characteristic type III isotherm, indicating both Fe<sub>2</sub>O<sub>3</sub>-S-X and Fe<sub>2</sub>O<sub>3</sub>-B are mesoporous materials (Fig. S4). The average pore size and the specific surface area of Fe<sub>2</sub>O<sub>3</sub>-S-X and Fe<sub>2</sub>O<sub>3</sub>-B are confirmed, listed in the Table S1.

### 3.2. Defect characteristic

The defects of the samples were first characterized by positron annihilation techniques. As a mature technique for analyzing cation defects in solids, positron annihilation spectra can precisely give information about the size, type and relative concentration of various surface or bulk cation

defects by analyzing the positron lifetime and intensity, even if defect concentration at the parts–per–million level [37]. As shown in Table 1 and Fig. 3a, all samples exhibit three positron lifetime components,  $\tau_1$ ,  $\tau_2$  and  $\tau_3$ , with relative intensities of  $I_1$ ,  $I_2$ , and  $I_3$ . The longest component ( $\tau_3$ ) of all samples mainly arises from positrons annihilation in the crystal boundary. The shortest one ( $\tau_1$ ) is attributed to the free annihilation of positrons in perfect crystal without defects. However, in actual tests, the average electron density is reduced due to inevitable small size defects (like monovacancies, etc.) in the system, resulting in an elongated of  $\tau_1$  [38]. Here, the measured  $\tau_1$  for Fe<sub>2</sub>O<sub>3</sub>–S–X and Fe<sub>2</sub>O<sub>3</sub>–B is around 183 ps (Table 2), both of which should correspond to the isolated Fe vacancy, according to the positron lifetime values. Compared with small size defects, larger size defects will lead to lower average electron density, thereby reducing the annihilation rate and increasing the positron lifetime [39]. Thus, the second component ( $\tau_2$ ) for Fe<sub>2</sub>O<sub>3</sub>–S–X and Fe<sub>2</sub>O<sub>3</sub>–B can be assigned to positrons trapped by larger size defects, i.e. Fe<sup>3+</sup>–oxygen vacancy cluster defects. These results imply the presence of isolated Fe vacancy and Fe<sup>3+</sup>–oxygen vacancy clusters in all of the samples.

The relative concentration ratio of the large size  $Fe^{3+}$ —oxygen vacancy cluster defects to the smaller size isolated Fe vacancy defects can be obtained according to the relative intensity (I) of positron lifetime. Among all of the samples,  $Fe_2O_3$ —B exhibits the lowest relative concentration ratio of  $I_2$  to  $I_1$  ( $I_2/I_1$ ), 0.38, indicating that the concentration of large size defects is significantly lower than that of smaller size defects. In comparison, the values of  $I_2/I_1$  for  $Fe_2O_3$ —S—X are higher, proving that the relative concentration ratio of large size defects to smaller size defects can be tuned by introducing 2, 2'—bpy into the synthesis system. Here, we noticed that when the amount of 2, 2'—bpy introduced is 80 mg, the value of  $I_2/I_1$  reaches the highest (1.36). At this time, the relative concentration of large size defects accounts for over 50% of the total defects, which means

that large size defects have become the predominant ones for the Fe<sub>2</sub>O<sub>3</sub>–S–80.

To understand the distribution of defects in the material, we calculated the total energies,  $E_{\text{tot}}$ , of α-Fe<sub>2</sub>O<sub>3</sub> with different types of defect on the surface or in the bulk, including a α-Fe<sub>2</sub>O<sub>3</sub> with Fe<sup>3+</sup>-oxygen vacancy cluster defect on the surface (Model 1), a α-Fe<sub>2</sub>O<sub>3</sub> with Fe<sup>3+</sup>-oxygen vacancy cluster defect in the bulk (Model 2), a  $\alpha$ -Fe<sub>2</sub>O<sub>3</sub> with an isolated Fe vacancy defect on the surface (Model 3), and a  $\alpha$ -Fe<sub>2</sub>O<sub>3</sub> with an isolated Fe vacancy defect in the bulk (Model 4). It can be seen from Fig. 3b, large size Fe<sup>3+</sup>-oxygen vacancy cluster defects tend to exist on the surface of α-Fe<sub>2</sub>O<sub>3</sub>, while the smaller size isolated Fe vacancy defects are more stable in the bulk of  $\alpha$ -Fe<sub>2</sub>O<sub>3</sub>. To further confirm the distribution of the cation defects in  $\alpha$ -Fe<sub>2</sub>O<sub>3</sub>, we measured the surface charge of the samples by zeta-potentials. It is worth to note that the formation of cation defects resulted in many dangling O bonds, which could accommodate electrons. Thus, if the Fe<sup>3+</sup>-oxygen vacancy cluster defects and the isolated Fe vacancy defects indeed mainly exist on the surface and in the bulk of α-Fe<sub>2</sub>O<sub>3</sub>, respectively, the amount of surface negative charge will raise as the relative concentration of the Fe<sup>3+</sup>-oxygen vacancy cluster defect increases. Zeta-potential of both Fe<sub>2</sub>O<sub>3</sub>-B and Fe<sub>2</sub>O<sub>3</sub>-S-X at different pH were tested (Fig. 3c), Fe<sub>2</sub>O<sub>3</sub>-S-X obvious have smaller pH values at isoelectric point, which indicates that there are more dangling O bonds on the surface of Fe<sub>2</sub>O<sub>3</sub>-S-X. When the pH is close to neutral, the order of the amount of surface negative charge for the five samples is Fe<sub>2</sub>O<sub>3</sub>-S-80> Fe<sub>2</sub>O<sub>3</sub>-S-110> Fe<sub>2</sub>O<sub>3</sub>-S-50> Fe<sub>2</sub>O<sub>3</sub>-S-20> Fe<sub>2</sub>O<sub>3</sub>-B, which is consistent with the relative concentration of Fe<sup>3+</sup>-oxygen vacancy cluster defect in the five samples, verifying that large size cation defects mainly exist on the surface of the Fe<sub>2</sub>O<sub>3</sub> and smaller size cation defects mainly exist in bulk of the Fe<sub>2</sub>O<sub>3</sub>. In addition, the HR-TEM images shows that there are a large number of defects on the surface of Fe<sub>2</sub>O<sub>3</sub>-S-X (Fig. 3d); on the contrary, almost no defects are observed on the surface of Fe<sub>2</sub>O<sub>3</sub>-B

(Fig. 3e), which more intuitively verifies the judgment on the location of different cation defects.

Although the positron annihilation has confirmed that the surface defects in these samples are mainly Fe<sup>3+</sup>-oxygen vacancy clusters, the anion defects (i.e. oxygen vacancies) on the surface of the samples cannot be ignored, because the oxygen vacancy has been widely recognized as the one of the important factors influence catalytic activity of materials. Thus, we monitored the oxygen vacancy defects of the samples using electron spin resonance (ESR) spectra. As shown in Fig. S5a. all samples exhibit a similar ESR signal (g = 1.99), corresponding to the paramagnetic oxygen vacancies, as documented in previous references (e.g., BiVO<sub>4</sub>, SrTiO<sub>3</sub>, etc.) [40,41]. The peak intensities of all samples are same, indicating that the oxygen vacancy concentrations in these samples are similar. To further determine the difference in oxygen vacancy concentration of the samples, we conducted an in-depth analysis of the O<sub>1s</sub> high resolution XPS spectra (Fig. S5b). The O<sub>1s</sub> spectra of all samples can be fitted into three Gaussian peaks. Among these peaks, the peak at 531.9 eV is associated with the O<sup>2-</sup> in the oxygen vacancy of transition metal oxide surface, and the intensity of the peak is proportional to the concentration of oxygen vacancies [42]. Here, we found that the peak intensities of these samples are also similar, confirming that the oxygen vacancy concentrations of different samples are same, consistent with the conclusion of ESR.

Overall, a series of  $\alpha$ -Fe<sub>2</sub>O<sub>3</sub> samples with similar oxygen vacancy defect concentration but different relative concentration ratio of large size surface cation defects (LSCD) to smaller size bulk cation defects (SBCD) were successfully fabricated, which could serve as ideal models, to explore the optimum cation defects that contribute to the improvement of photocatalytic performance.

### 3.3. Photocatalytic performance and stability

The photocatalytic activities of the Fe<sub>2</sub>O<sub>3</sub>–S–X and Fe<sub>2</sub>O<sub>3</sub>–B were compared by examining their

catalytic effects on the degradation of Bisphenol A (BPA) under simulated visible light irradiation ( $\lambda \ge 420$  nm). As the model target compound, BPA is a rigorously regulated environmental contaminant with endocrine-disrupting effects. The degradation ratio  $(\eta)$  of BPA was defined using  $\eta$  (%) =  $(1 - C/C_0) \times 100\%$ , where C and  $C_0$  depict the BPA concentrations in the effluent and the feeding stream, respectively. No measurable degradation of BPA was observed in the absence of the photocatalysis nor in the presence of the photocatalysis but without visible light irradiation, which reveals that the decrease in BPA concentration is entirely derived from photocatalysis progress (Fig. S6). As shown in Fig. 4a, Fe<sub>2</sub>O<sub>3</sub>-S-X exhibit much higher BPA degradation ratio than Fe<sub>2</sub>O<sub>3</sub>-B at the same catalyst concentration, indicating their higher photocatalytic activity. After 6 h of visible light irradiation, Fe<sub>2</sub>O<sub>3</sub>-S-80 with the highest relative concentration ratio of LSCD to SBCD exhibits the highest  $\eta$  value (95.2%), which is superior to Fe<sub>2</sub>O<sub>3</sub>-S-110 (77.9%), Fe<sub>2</sub>O<sub>3</sub>-S-50 (69.2%), Fe<sub>2</sub>O<sub>3</sub>-S-20 (58.0%) and Fe<sub>2</sub>O<sub>3</sub>-B (28.8%). Here, we found that the order of  $\eta$  values is consistent with the order of relative concentration ratio of LSCD to SBCD, which reveals that the increase in the relative concentration ratio of LSCD to SBCD contributes to the improvement of photocatalytic activity of the α–Fe<sub>2</sub>O<sub>3</sub>. Furthermore, the total organic carbon (TOC) data further show the greater photocatalytic activity of Fe<sub>2</sub>O<sub>3</sub>-S-X (Fig. 4b). Upon visible light irradiation for 12 h, exceeded 90% of BPA was mineralized when using Fe<sub>2</sub>O<sub>3</sub>–S–80 as a catalyst. In contrast, the mineralization yield by Fe<sub>2</sub>O<sub>3</sub>–B was only 22.3%. To further investigate the difference in photocatalytic activity, surface area normalized conversion for Fe<sub>2</sub>O<sub>3</sub>–S–X and Fe<sub>2</sub>O<sub>3</sub>–B were performed (based on the specific surface area data in Tab. S1), which helped to compare the photon utilization efficiency of catalysts. It can be seen from Fig. 4c and 4d that Fe<sub>2</sub>O<sub>3</sub>–S–X still has a greater photocatalytic activity and a higher reaction rate when absorbing the same amount of photons, which not only indicates that Fe<sub>2</sub>O<sub>3</sub>-S-X has greater

photon utilization efficiency, but also confirms the change in defect characteristics is a major factor affecting the change in catalyst activity.

Obviously, Fe<sub>2</sub>O<sub>3</sub>–S–80 shows the highest photocatalytic activity in all samples, and it was consequently chosen as a research object for the photocatalytic stability test, which is especially important for judging whether the contribution of cation defects in photocatalysis is persistent or not. As shown in Fig. S7, the photocatalytic activity of Fe<sub>2</sub>O<sub>3</sub>–S–80 can remain stable in the first six cycles, indicating that cation defects can provide a continuous contribution to photocatalysts. We collected the Fe<sub>2</sub>O<sub>3</sub>–S–80 sample after cycle reaction and studied it by TEM. TEM image (Fig. S8a) clearly shows that the nanorod architectures remain intact after reaction, indicating that the sample is anti–photo corrosive during the reaction. Moreover, FT–IR was used to investigate the changes in the structure of the Fe<sub>2</sub>O<sub>3</sub>–S–80 during the reaction. From Fig. S8b, the cyclically reacted sample has the same absorption band as the original one, which implies that Fe<sub>2</sub>O<sub>3</sub>–S–80 can keep a stable internal structure during multiple photocatalytic reactions. A great anti-corrosive surface and a stable internal structure are beneficial to the stable existence of the defect structure, which is a prerequisite for ensuring the long-term effect of the cation defect.

### 3.4. Photocatalysis mechanism

To explain the higher photocatalytic activity of Fe<sub>2</sub>O<sub>3</sub>–S–X than Fe<sub>2</sub>O<sub>3</sub>–B, we first investigated their light adsorption property by UV–vis diffuse reflectance spectra (Fig. 5a). Compared with the Fe<sub>2</sub>O<sub>3</sub>–B, adsorption edges of the Fe<sub>2</sub>O<sub>3</sub>–S–X are red–shifted, meaning that the increase of relative concentration ratio of LSCD to SBCD can extend the adsorption range of visible light of the materials. To further confirm that the difference in light adsorption property comes from the change in relative concentration ratio of LSCD to SBCD, we calculated the density of state (DOS) of  $\alpha$ –Fe<sub>2</sub>O<sub>3</sub> with different defects (using Model 1 and Model 4). According to the calculation results

(Fig. 5b), the band gap of  $\alpha$ -Fe<sub>2</sub>O<sub>3</sub> has slightly narrowed when the SBCD changed to LSCD, which not only indicates that the difference in defects can cause the band gap to change, but also confirms that the extension of the light adsorption range is derived from the increase of the relative concentration ratio of LSCD to SBCD.

The band gap  $(E_g)$  structure for the samples was estimated by Tauc plot. As shown in Fig. S9a, Fe<sub>2</sub>O<sub>3</sub>-S-X samples have narrower band gap than the Fe<sub>2</sub>O<sub>3</sub>-B, which is consistent with the calculated results, meaning that the surface electrons of the Fe<sub>2</sub>O<sub>3</sub>-S-X samples are more easily photoexcited. The valence band (VB) of both Fe<sub>2</sub>O<sub>3</sub>-S-X and Fe<sub>2</sub>O<sub>3</sub>-B was analyzed with XPS valence spectra (Fig. S9b). Correspondingly, conduction band (CB) position of the samples was determined by  $E_{CB} = E_{VB} - E_g$ . As shown in Fig. 5c, both the VB width and the CB minimum energies of Fe<sub>2</sub>O<sub>3</sub>-S-X are significantly up-shifted as the relative concentration ratio of LSCD to SBCD increases. From the perspective of kinetic requirements for semiconductor photocatalytic reactions, the raised VB width as well as the up-shifting CB minimum are both beneficial to enhance photocatalytic efficiency. A raised VB width can result in a higher mobility of photogenerated holes, while an up-shifting CB minimum can also enhance the transfer ability of photogenerated electrons, which helps to avoid recombination of photoinduced e-h pairs [43]. Here, the transfer properties of photogenerated carrier in Fe<sub>2</sub>O<sub>3</sub>-S-X and Fe<sub>2</sub>O<sub>3</sub>-B were investigated by EIS Nyquist plot. As shown in Fig. 5d, EIS Nyquist plots of the samples are all well simulated to the equivalent electrical circuit. The radius of the arc in the middle-frequency region represents the interfacial charge-transfer resistance ( $R_{ct}$ ), which reflects the efficiency of charge carrier transfer, and it is one of the most important factors affecting catalytic activity. Evidently, all Fe<sub>2</sub>O<sub>3</sub>-S-X samples exhibit smaller R<sub>ct</sub> values (Table S2) than that of Fe<sub>2</sub>O<sub>3</sub>-B under visible light irradiation, which corroborates that the photogenerated charge carriers of Fe<sub>2</sub>O<sub>3</sub>–S–X

have higher transfer activity. Among these samples, Fe<sub>2</sub>O<sub>3</sub>–S–80 shows the smallest  $R_{ct}$  value, which not only echoes the most excellent photocatalytic activity, but also confirms that the relative concentration ratio of LSCD to SBCD in  $\alpha$ –Fe<sub>2</sub>O<sub>3</sub> is highly correlated with its charge carrier transfer ability. Room temperature steady-state PL spectroscopy was employed to clarify the photoinduced e–h separation ability of Fe<sub>2</sub>O<sub>3</sub>–S–X and Fe<sub>2</sub>O<sub>3</sub>–B (Fig. 5e). Compared with Fe<sub>2</sub>O<sub>3</sub>–B, Fe<sub>2</sub>O<sub>3</sub>–S–X exhibits PL quenching phenomenon, which can be assigned to their greater electron photoextraction efficiency and lower e–h recombination efficiency. Meanwhile, the order of PL peak intensity is Fe<sub>2</sub>O<sub>3</sub>–B> Fe<sub>2</sub>O<sub>3</sub>–S–20> Fe<sub>2</sub>O<sub>3</sub>–S–50> Fe<sub>2</sub>O<sub>3</sub>–S–110> Fe<sub>2</sub>O<sub>3</sub>–S–80, which is consistent with the band gap order, demonstrating that a narrow band gap structure and a high e–h separation efficiency can be achieved by increasing the relative concentration ratio of LSCD to SBCD.

Besides of improving the transfer abitily of charge carrier, from the thermodynamic requirements of the photocatalytic oxidation process, the elevation of the CB minimum also makes the photogenerated electrons easier to react with O<sub>2</sub> molecules adsorbed on the material surface to form reactive oxygen species (ROS). Here, we compared the ROS production activity between the Fe<sub>2</sub>O<sub>3</sub>–S–X (take Fe<sub>2</sub>O<sub>3</sub>–S–80 as an example) and Fe<sub>2</sub>O<sub>3</sub>–B samples under visible light irradiation. The DMPO spin-trapping ESR analyses are used to monitor the reactive radicals during the photocatalysis processes. As shown in Fig. 6a, both catalysts are capable to produce O<sub>2</sub><sup>--</sup>. Compared with Fe<sub>2</sub>O<sub>3</sub>–B, peak intensity of Fe<sub>2</sub>O<sub>3</sub>–S–80 is slightly stronger, indicating a higher O<sub>2</sub><sup>--</sup> concentration. It is well–known that O<sub>2</sub><sup>--</sup> are formed by the combination of O<sub>2</sub> molecules with electrons (reactions 1–2), thus a higher concentration of O<sub>2</sub><sup>--</sup> not only demonstrates that the Fe<sub>2</sub>O<sub>3</sub>–S–80 has a more prominent charge carrier separation capability, but also means that O<sub>2</sub> molecules have a higher reactivity on the surface of the Fe<sub>2</sub>O<sub>3</sub>–S–80. To further uncover the

difference in carrier separation activities between Fe<sub>2</sub>O<sub>3</sub>–S–80 and Fe<sub>2</sub>O<sub>3</sub>–B, steady-state SPV (SS-SPV) was carried out. As shown in Fig. 6b, both two samples exhibited an SS-SPV response in the range of 300 to 550 nm with a main SPV peak around 370 nm, which can be attributed to the band-to-band electronic transition [44]. Apparently, Fe<sub>2</sub>O<sub>3</sub>–S–80 shows a stronger SS-SPV response than Fe<sub>2</sub>O<sub>3</sub>–B, which not only indicates that Fe<sub>2</sub>O<sub>3</sub>–S–80 surface can produce more photogenerated electrons, but also proves that increasing the relative concentration ratio of LSCD to SBCD can effectively promote the separation of charge carriers.

Photocatalysts 
$$+ h \nu \rightarrow e + h$$
 (1)

$$O_2 + e \rightarrow O_2^{\bullet -}$$
 (2)

$$O_2^{-} + 2H^+ + e \rightarrow H_2O_2$$
 (3)

$$H_2O_2 + e \rightarrow \bullet OH + OH^-$$
 (4)

$$h + OH^- \rightarrow \bullet OH$$
 (5)

The activation property of  $O_2$  molecules on the surface of  $Fe_2O_3$ –S–80 and  $Fe_2O_3$ –B was investigated (using Model 1 and Model 4). Compared with Model 4,  $O_2$  molecules have higher adsorption energy ( $E_{ads}$ ) on the surface of Model 1 (Fig. 6c), which reveals that increasing the relative concentration ratio of LSCD to SBCD can promote the adsorption of  $O_2$  molecules on the surface of  $\alpha$ – $Fe_2O_3$ . According to the calculation results, we can infer that the surface of  $Fe_2O_3$ –S–S0 can adsorb much more  $O_2$  molecules than  $Fe_2O_3$ –S, which means that  $Fe_2O_3$ –S–S0 has a greater potential for generating  $O_2$ –C0, consistent with previous ESR results in fig. 6a. Indeed, the O–O bond length in Model 1 is 1.353 Å, longer than that in Model 4 (1.337 Å), indicating that increasing the relative concentration ratio of LSCD to SBCD could remarkably weaken the O–O bonds and thereby promoting the activation of surface  $O_2$  molecules. Furthermore, the Bader effective charge on the  $O_2$  molecules was calculated.  $O_2$  molecules adsorb on the surface of Model

1 will obtain more electrons (0.76 e) than adsorb on the surface of Model 4 (0.34 e), which not only verifies the stronger charge transfer activity between the  $Fe_2O_3-S-80$  surface and  $O_2$  molecules, but also supports the conclusion that  $Fe_2O_3-S-80$  can generate more  $O_2^{\bullet}$ .

Fig. 6d shows that Fe<sub>2</sub>O<sub>3</sub>–S–80 produces much more •OH than Fe<sub>2</sub>O<sub>3</sub>–B during the photocatalysis process. Due to the fact that the potential energy of VB holes (Fig. 5c) from both Fe<sub>2</sub>O<sub>3</sub>–S–80 and Fe<sub>2</sub>O<sub>3</sub>–B are lower than that of OH<sup>-</sup>/•OH (1.99 eV, NHE) and H<sub>2</sub>O/•OH (2.37 eV, NHE), it can be confirmed •OH is not come from the reaction 5, which should be generated via the transformation of O<sub>2</sub><sup>--</sup> (reactions 3–4) [45,46]. Thus, a higher concentration of •OH not only again illustrates that Fe<sub>2</sub>O<sub>3</sub>–S–80 have a stronger charge carrier separation ability, but also suggests that the photogenerated electrons from Fe<sub>2</sub>O<sub>3</sub>–S–80 have a longer survival life. To confirm the survival life of photogenerated electrons, we measured time–resolved PL decay curves to monitor the dynamics of photogenerated charge carrier in the two samples. From Fig. 6e, the PL peak decay of Fe<sub>2</sub>O<sub>3</sub>–S–80 is much slower than that of the Fe<sub>2</sub>O<sub>3</sub>–B, which proves that the photogenerated electrons from Fe<sub>2</sub>O<sub>3</sub>–S–80 have longer lifetime than that of Fe<sub>2</sub>O<sub>3</sub>–B. Both of PL peak decay curves were reasonably fitted by a double-exponential model, according to the following equation:

$$I = A_1 \exp(-t/\tau_1) + A_2 \exp(-t/\tau_2)$$
 (6)

where I is the PL intensity,  $\tau$  repesents the decay times, and A is the corresponding magnitude. The slow component ( $\tau$ ) was due to the radiative emission via indirect recombination, while the faster component ( $\tau$ ) can be ascribed to the radiative emission of direct interband exciton recombination. Based on the fitting results, the increased relative concentration ratio of LSCD to SBCD exacerbates the indirect recombination process of photogenerated carriers, thereby effectively suppressing the direct recombination of e-h pairs and prolonging the lifetime of photogenerated

electrons. To further grasp the dynamic behaviors of the charge carrier of Fe<sub>2</sub>O<sub>3</sub>–S-80 and Fe<sub>2</sub>O<sub>3</sub>–B, transient-state SPV (TS-SPV) was measured. It can be seen from fig. 6f the TS-SPV response signals for both samples are positive, indicating that photogenerated holes accumulate at the surface of materials. Obviously, the lifetime of Fe<sub>2</sub>O<sub>3</sub>–S-80 is longer than that of Fe<sub>2</sub>O<sub>3</sub>–B, verifing that the photogenerated carriers from Fe<sub>2</sub>O<sub>3</sub>–S-80 have a longer survival life. Furthermore, the signal of Fe<sub>2</sub>O<sub>3</sub>–S-80 is stronger than that of Fe<sub>2</sub>O<sub>3</sub>–B, which again demonstrates that the Fe<sub>2</sub>O<sub>3</sub>–S-80 has a greater separation efficiency of e-h pairs. In summary, the results of experimental and theoretical calculations have determined that the difference in photocatalytic performance is caused by the change of the relative concentration of cation defects of  $\alpha$ –Fe<sub>2</sub>O<sub>3</sub>. The increase of the relative concentration ratio of LSCD to SBCD not only improves the separation ability of e-h pairs in  $\alpha$ –Fe<sub>2</sub>O<sub>3</sub>, prolongs the carrier lifetime, but also promotes the generation of ROS, which contributes to the improvement of photocatalytic activity of catalyst.

### 3.5. Cation defect—dependent photocatalytic degradation pathways

Differences in the predominant forms of cation defect lead to different ROS formation ability, which may cause different degradation pathways. The intermediates formed during BPA photocatalytic degradation were analyzed by LC/MS/MS (Fig. 7a and 7b). We detected the product ion at m/z (number of protons/number of charges) 227 in both experiments with Fe<sub>2</sub>O<sub>3</sub>–S–80 and Fe<sub>2</sub>O<sub>3</sub>–B and identified it as the deprotonated molecule [(M–H)] of BPA. When Fe<sub>2</sub>O<sub>3</sub>–S–80 worked as the photocatalyst, four product ions (m/z 163, 143, 133, 121) were detected and identified based on the previous reports (Fig. 7c) [47,48]. We found that all intermediates appeared early in the reaction and increased rapidly within 4 h, but as the reaction proceeded, their concentrations gradually decreased until they almost disappeared (< 1%). In comparsion, only two product ions (m/z 243, 133) were identified when Fe<sub>2</sub>O<sub>3</sub>–B was used as the photocatalyst (Fig. 7d)

[18]. From Fig. 7b, the concentration of the intermediate m/z 133 increased consistently during the reaction and gradually decreased after 8 h. On the contrary, the concentration of the other product ion did not decrease significantly after reaching the maximum value, but continued to remain stable until the end of the reaction, which means that Fe<sub>2</sub>O<sub>3</sub>–B could not degrade BPA completely. The patterns shown in Fig. 7a and 7b are consistent with the results of TOC removal (Figure 4b) and clearly show that Fe<sub>2</sub>O<sub>3</sub>–S–80 with higher relative concentration ratio of LSCD to SBCD defect is more effective in degrading BPA into small organic acids and eventually into inorganic molecules.

### 3.6. Speculation on the formation mechanism of 2, 2'-bpy induced surface defects

In this work, we discovered for the first time that 2, 2'-bpy can tune the relative concentration ratio of LSCD to SBCD in  $\alpha$ -Fe<sub>2</sub>O<sub>3</sub>. Herein, we speculate on the causes of bpy-induced an increase in LSCD concentration. Compared with the synthesis system without 2, 2'-bpy, the introduction of 2, 2'-bpy leads to a decrease in the concentration of Fe<sup>3+</sup> in the reaction system, which is due to the coordination of 2, 2'-bpy with Fe<sup>3+</sup> (Fe(bpy)<sup>3+</sup>) limits the movement of Fe<sup>3+</sup>. It is well known that the crystal growth process is divided into two stages: nucleation process and Ostwald ripening process. Herein, the decrease in the relative concentration of Fe<sup>3+</sup> slows down the Ostwald ripening process required for crystal formation. A slower Ostwald ripening process can effectively avoid the appearance of bulk defects, which contributes to perfect crystal formation. As the crystal formation process progresses, many Fe(bpy)<sup>3+</sup> ions adhere to the surface of the  $\alpha$ -Fe<sub>2</sub>O<sub>3</sub> crystal, which hinder the crystal continuing to grow in some positions due to the steric effect, resulting in surface defects. Also, for this reason, we can observe that the relative concentration ratio of LSCD to SBCD in  $\alpha$ -Fe<sub>2</sub>O<sub>3</sub> is proportional to the amount of 2, 2'-bpy. However, when the amount of 2, 2'-bpy reaches 110 mg, we found that the relative concentration ratio of LSCD slight

decline, which may be due to the fact that excess 2, 2'-bpy severely reduces the concentration of Fe<sup>3+</sup> in the early stage of crystal growth. Although a slow Ostwald ripening process helps to avoid the formation of bulk defects, a significant decrease in the concentration of Fe<sup>3+</sup> still leads to the formation of partial bulk defects, such that the relative concentration ratio of LSCD to SBCD of a slight reduce phenomenon occurs.

#### 4. Conclusion

In summary, this work presents a novel method of tuning the cation defects of  $\alpha$ –Fe<sub>2</sub>O<sub>3</sub> nanostructures: the introduction of 2, 2'–bpy. By controlling the amount of 2, 2'–bpy introduced, the regulation of the relative concentration ratio of large size surface cation defects (LSCD) to smaller size bulk cation defects (SBCD) of  $\alpha$ –Fe<sub>2</sub>O<sub>3</sub> can be achieved. Compare with SBCD, LSCD are more helpful to enhance the photocatalytic activity of  $\alpha$ –Fe<sub>2</sub>O<sub>3</sub>. We demonstrated theoretically and experimentally that increasing the relative concentration ratio of LSCD to SBCD in  $\alpha$ –Fe<sub>2</sub>O<sub>3</sub> nanostructures not only significantly improves the e–h separation efficiency, but also enhances the activity of O<sub>2</sub> molecules on the surface of the materials, thus significantly enhance the photocatalytic efficiency and ROS generation activity. These findings provide fundamental insight into the role of cation defects in photocatalysis through cation defects engineering. The regulation strategy and understand of action mechanism on cation defects in this work may also be applicable to other semiconductor photocatalysts, such as ZnO, BiOX (X= Cl, Br, I), etc.

#### **Declaration of interests**

The authors declare that they have no known competing financial interests or personal relationships that could have appeared to influence the work reported in this paper.

## Acknowledgements

This work was supported by the National Natural Science Foundation of China (grant 21701125, 21171128, 21271108 and 51702236), Key Project Natural Science Foundation of Tianjin (18JCZDJC39800) and the project of science and technology of Tianjin (18ZXSZSF00040, 18KPXMSF00080, 18PTZWHZ00010).

#### References

- [1] J. Kou, C. Lu, J. Wang, Y. Chen, Z. Xu, R. S. Varma, Selectivity enhancement in heterogeneous photocatalytic transformations, Chem. Rev. 117 (2017) 1445–1514. DOI: 10.1021/acs.chemrev.6b00396.
- [2] T. Hisatomi, K. Domen, Reaction systems for solar hydrogen production via water splitting with particulate semiconductor photocatalysts, Nat. Catal. 2 (2019) 387–399. DOI: 10.1038/s41929-019-0242-6.
- [3] A. Kubacka, M. Fernández-García, G. Colón, Advanced nanoarchitectures for solar photocatalytic applications, Chem. Rev. 112 (2012) 1555–1614. DOI: 10.1021/cr100454n.
- [4] X. Wang, L. Chen, S. Y. Chong, M. A. Little, Y. Wu, W. Zhu, R. Clowes, Y. Yan, M. A. Zwijnenburg, R. S. Sprick, A. I. Cooper, Sulfone-containing covalent organic frameworks for photocatalytic hydrogen evolution from water, Nat. Chem. 10 (2018) 1180–1189. DOI: 10.1038/s41557-018-0141-5.
- [5] Z. Bian, F. Cao, J. Zhu, H. Li, Plant uptake-assisted round-the-clock photocatalysis for complete purification of aquaculture wastewater using sunlight, Environ. Sci. Technol. 49 (2015) 2418–2424. DOI: 10.1021/es505540x.
- [6] L. Lin, Z. Yu, X. Wang, Crystalline carbon nitride semiconductors for photocatalytic water splitting, Angew. Chem. Int. Ed. 58 (2019) 6164–6175. DOI: 10.1002/anie.201809897.
- [7] L. Wang, J. Wan, Y. Zhao, N. Yang, D. Wang, Hollow multi-shelled structures of Co<sub>3</sub>O<sub>4</sub> Dodecahedron with unique crystal orientation for enhanced photocatalytic CO<sub>2</sub> reduction, J. Am. Chem. Soc. 141 (2019) 2238–2241. DOI: 10.1021/jacs.8b13528.

- [8] S. Xiao, D. Zhang, D. Pan, W. Zhu, P. Liu, Y. Cai, G. Li, H. Li, A chloroplast structured photocatalyst enabled by microwave synthesis, Nat. Chem. 10 (2019) 1570. DOI: 10.1038/s41467-019-09509-y.
- [9] L. Cheng, Q. Xiang, Y. Liao, H. Zhang, CdS-based photocatalysts, Energy Environ. Sci. 11 (2018) 1362–1391. DOI: 10.1039/C7EE03640J.
- [10] X. Wang, X. Zhao, D. Zhang, G. Li, H. Li, Microwave irradiation induced UIO-66-NH<sub>2</sub> anchored on graphene with high activity for photocatalytic reduction of CO<sub>2</sub>, Appl. Catal. B: Environ. 228 (2018) 47–53. DOI: 10.1016/j.apcatb.2018.01.066.
- [11] J. Ran, W. Guo, H. Wang, B. Zhu, J. Yu, S. Z. Qiao, Metal-free 2D/2D phosphorene/g-C<sub>3</sub>N<sub>4</sub> Van Der Waals heterojunction for highly enhanced visible-light photocatalytic H<sub>2</sub> production, Adv. Mater. 30 (2018) 1800128. DOI: 10.1002/adma.201800128.
- [12] Y. Bi, S. Ouyang, N. Umezawa, J. Cao, J. Ye, Facet effect of single-crystalline Ag<sub>3</sub>PO<sub>4</sub> sub-microcrystals on photocatalytic proerties, J. Am. Chem. Soc. 133 (2011) 6490–6492. DOI: 10.1021/ja2002132.
- [13] L. Li, J. Yan, T. Wang, Z. Zhao, J. Zhang, J. Gong, N. Guan, Sub-10 nm rutile titanium dioxide nanoparticles for efficient visible-light-driven photocatalytic hydrogen, Nat. Common. 6 (2015) 5881. DOI: 10.1038/ncomms6881.
- [14] Y. Wang, J. Cai, M. Wu, J. Chen, W. Zhao, Y. Tian, T. Ding, J. Zhang, Z. Jiang, X. Li, Rational construction of oxygen vacancies onto tungsten trioxide to improve visible light photocatalytic water oxidation reaction, Appl. Catal. B: Environ. 239 (2018) 398–407. DOI: 10.1016/j.apcatb.2018.08.029.
- [15] H. Li, J. Li, Z. Ai, F. Jia, L. Zhang, Oxygen vacancy-mediated photocatalysis of BiOCl: reactivity, selectivity, and perspectives, Angew. Chem. Int. Ed. 57 (2018) 122–138. DOI:

- 10.1002/anie.201705628.
- [16] H. Wang, J. Zhang, X. Hang, X. Zhang, J. Xie, B. Pan, Y. Xie, Half-metallicity in single-layered manganese dioxide nanosheets by defect engineering, Angew. Chem. Int. Ed. 54 (2015) 1195–1199. DOI: 10.1002/anie.201410031.
- [17] Q. Wang, Y. Lei, D. Wang, Y. Li, Defect engineering in earth-abundant electrocatalysts for CO<sub>2</sub> and N<sub>2</sub> reduction, Energy Environ. Sci. 12 (2019) 1730–1750. DOI: 10.1039/C8EE03781G.
- [18] S. Guo, X. Zhu, H. Zhang, B. Gu, W. Chen, L. Liu, P. J. J. Alvarez, Improving photocatalytic water treatment through nanocrystal engineering: mesoporous nanosheet-assembled 3D BiOCl hierarchical nanostructures that induce unprecedented large vacancies, Environ. Sci. Technol. 52 (2018) 6872–6880. DOI: 10.1021/acs.est.8b00352.
- [19] J. Nowotny, M. A. Alim, T. Bak, M. A. Idris, M. Ionescu, K. Prince, M. Z. Sahdan, K. Sopian, M. A. M. Teridi, W. Sigmund, Defect chemistry and defect engineering of TiO<sub>2</sub>-based semiconductors for solar energy conversion, Chem. Soc. Rev. 44 (2015) 8424–8442. DOI: 10.1039/C4CS00469H.
- [20] J. Li, W. Zhang, M. Ran, Y. Sun, H. Huang, F. Dong, Synergistic integration of Bi metal and phosphate defects on hexagonal and monoclinic BiPO<sub>4</sub>: enhanced photocatalysis and reaction mechanism, Appl. Catal. B: Environ. 243 (2019) 313–321. DOI: 10.1016/j.apcatb.2018.10.055.
- [21] M. Faraji, M. Yousefi, S. Yousefzadeh, M. Zirak, N. Naseri, T. H. Jeon, W. Choi, A. Z. Moshfegh, Two-dimensional materials in semiconductor photoelectrocatalytic systems for water splitting, Energy Environ. Sci. 12 (2019) 59–95. DOI: 10.1039/C8EE00886H.
- [22] F. Lei, Y. Sun, K. Liu, S. Gao, L. Liang, B. Pan, Y. Xie, Oxygen vacancies confined in

- ultrathin indium oxide porous sheets for promoted visible-light water splitting, J. Am. Chem. Soc. 136 (2014) 6826–6829. DOI: 10.1021/ja501866r.
- [23] B. Ohtani, Titania photocatalysis beyond recombination: a critical review, Catalysts 3 (2013) 942–953. DOI: 10.3390/catal3040942.
- [24] D. Chen, Z. Wang, T. Ren, H. Ding, W. Yao, R. Zong, Y. Zhu, Influence of defects on the photocatalytic activity of ZnO, J. Phys. Chem. C 118 (2014) 15300–15307. DOI: 10.1021/jp5033349.
- [25] B. Wang, X. Wang, L. Lu, C. Zhou, Z. Xin, J. Wang, X. Ke, G. Sheng, S. Yan, Z. Zou, Oxygen-vacancy-activated CO<sub>2</sub> splitting over amorphous oxide semiconductor photocatalyst, ACS Catal. 8 (2018) 516–525. DOI: 10.1021/acscatal.7b02952.
- [26] D. Cui, L. Wang, K. Xu, L. Ren, L. Wang, Y. Yu, Y. Du, W. Hao, Band-gap engineering of BiOCl with oxygen vacancies for efficient photooxidation properties under visible-light irradiation, J. Mater. Chem. A 6 (2018) 2193–2199. DOI: 10.1039/C7TA09897A.
- [27] G. Li, G. R. Blake, T. T. M. Palstra, Vacancies in functional materials for clean energy storage and harvesting: the perfect imperfection, Chem. Soc. Rev. 46 (2017) 1693–1706. DOI: 10.1039/C6CS00571C.
- [28] X. Xue, R. Chen, H. Chen, Y. Hu, Q. Ding, Z. Liu, L. Ma, G. Zhu, W. Zhang, Q. Yu, J. Liu, J. Ma, Z. Jin, Oxygen vacancy engineering promoted photocatalytic ammonia synthesis on ultrathin two-dimensional bismuth oxybromide nanosheets, Nano Lett. 18 (2018) 7372–7377. DOI: 10.1021/acs.nanolett.8b03655.
- [29] J. Hui, G. Zhang, C. Ni, J. T. S. Irvine, Promoting photocatalytic H<sub>2</sub> evolution by tuning cation deficiency in La and Cr co-doped SrTiO<sub>3</sub>, Chem. Commun. 53 (2017) 10038–10041. DOI: 10.1039/C7CC05144A.

- [30] X. Jiao, Z. Chen, X. Li, Y. Sun, S. Gao, W. Yan, C. Wang, Q. Zhang, Y. Lin, Y. Luo, Y. Xie, Defect-mediated electron-hole separation in one-unit-cell Znln<sub>2</sub>S<sub>4</sub> layers for boosted solar-driven CO<sub>2</sub> reduction, J. Am. Chem. Soc. 139 (2017) 7586–7594. DOI: 10.1021/jacs.7b02290.
- [31] M. J. Puska, R. M. Nieminen, Theory of positrons in solids and on solid surfaces, Rev. Mod. Phys. 66 (1994) 841–897. DOI: 10.1103/RevModPhys.66.841.
- [32] B. Barbiellini, M. J. Puska, T. Korhonen, A. Harju, T. Torsti, R. M. Nieminen, Calculation of positron states and annihilation in solids: a density-gradient-correction scheme, Phys. Rev. B: Condens. Matter Mater. Phys. 53 (1996) 16201–16213. DOI: 10.1103/PhysRevB.53.16201.
- [33] G. Kresse, J. Furthmuller, Efficient iterative schemes for ab initio total-energy calculations using a plane-wave basis set. Phys. Rev. B: Condens. Matter Mater. Phys. 54 (1996) 11169–11186. DOI: 10.1103/physrevb.54.11169.
- [34] J. P. Perdew, Y. Wang, Accurate and simple analytic representation of the electron-gas correlation energy. Phys. Rev. B: Condens. Matter Mater. Phys. 45 (1992) 13244–13249. DOI: 10.1103/PhysRevB.45.13244.
- [35] G. Henkelman, B. P. Uberuaga, H. Jonsson, A climbing image nudged elastic band method for finding saddle points and minimum energy paths, J. Chem. Phys. 113 (2000) 9901–9904. DOI: 10.1063/1.1329672.
- [36] S. Guo, J. Wang, Y. Chen, B. Gu, B. Shen, Vacancy associates evoked hematite mesocubes with enhanced efficiency in Li storage behaviors, J. Phys. Chem. C 122 (2018) 23377–23384. DOI: 10.1021/acs.jpcc.8b08283.
- [37] M. Kong, Y. Li, X. Chen, T. Tian, P. Fang, F. Zheng, X. Zhao, Tuning the relative concentration ratio of bulk defects to surface defects in TiO<sub>2</sub> nanocrystals leads to high

- photocatalytic efficiency, J. Am. Chem. Soc. 133 (2011) 16414–16417. DOI: 10.1021/ja207826q.
- [38] X. Liu, K. Zhou, L. Wang, B. Wang, Y. Li, Oxygen vacancy clusters promoting reducibility and activity of ceria nanorods, J. Am. Chem. Soc. 131 (2009) 3140–3141. DOI: 10.1021/ja808433d.
- [39] J. Li, X. Wu, W. Pan, G. Zhang, H. Chen, Vacancy-rich monolayer BiO<sub>2-x</sub> as a highly efficient UV, visible, and near-infrared responsive photocatalyst, Angew. Chem., Int. Ed. 57 (2018) 491–495. DOI: 10.1002/anie.201708709.
- [40] B. Zhang, L. Wang, Y. Zhang, Y. Ding, Y. Bi, Ultrathin FeOOH nanolayers with abundant oxygen vacancies on BiVO<sub>4</sub> photoanodes for efficient water oxidation, Angew. Chem., Int. Ed. 57 (2018) 2248–2252. DOI: 10.1002/anie.201712499.
- [41] H. Tan, Z. Zhao, W. Zhu, E. N. Coker, B. Li, M. Zheng, W. Yu, H. Fan, Z. Sun, Oxygen vacancy enhanced photocatalytic activity of pervoskite SrTiO<sub>3</sub>, ACS Appl. Mater. Interfaces 6 (2014) 19184–19190. DOI: 10.1021/am5051907.
- [42] Y. Lv, W. Yao, X. Ma, C. Pan, R. Zong, Y. Zhu, The surface oxygen vacancy induced visible activity and enhanced UV activity of a ZnO<sub>1-x</sub> photocatalyst, Catal. Sci. Technol. 3 (2013) 3136–3146. DOI: 10.1039/C3CY00369H.
- [43] M. Guan, C. Xiao, J. Zhang, S. Fan, R. An, Q. Cheng, J. Xie, M. Zhou, B. Ye, Y. Xie, Vacancy associates promoting solar-driven photocatalytic activity of ultrathin bismuth oxychloride nanosheets, J. Am. Chem. Soc. 135 (2013) 10411–10417. DOI: 10.1021/ja402956f.
- [44] Q. Li, X. Li, S. Wageh, A. A. Al-Ghamdi, J. Yu, CdS/graphene nanocomposite photocatalysts, Adv. Energy Mater. 5 (2015) 1500010. DOI: 10.1002/aenm.201500010.

- [45] J. Li, Z. Zhang, W. Cui, H. Wang, W. Cen, G. Johnson, G. Jiang, S. Zhang, F. Dong, The spatially oriented charge flow and photocatalysis mechanism on internal van der Waals heterostructures enhanced g-C<sub>3</sub>N<sub>4</sub>, ACS Catal. 8 (2018) 8376–8385. DOI: 10.1021/acscatal.8b02459.
- [46] L. Wang, S. Guo, Y. Chen, M. Pan, E. H. Ang, Z. Yuan, A mechanism investigation of how the alloying effect improves the photocatalytic nitrate reduction activity of bismuth oxyhalide nanosheets, ChemPhotoChem. DOI: 10.1002/cptc.201900217.
- [47] C. Wang, H. Zhang, F. Li, L. Zhu, Degradation and mineralization of bisphenol A by mesoporous Bi<sub>2</sub>WO<sub>6</sub> under simulated solar light irradiation, Environ. Sci. Technol. 44 (2010) 6843–6848. DOI: 10.1021/es101890w.
- [48] K. Lin, W. Liu, J. Gan, Oxidative removal of bisphenol A by manganese dioxide: Efficacy, products, and pathways, Environ. Sci. Technol. 43 (2009) 3860–3864. DOI: 10.1021/es900235f.

Table 1 Positron lifetime parameters of Fe<sub>2</sub>O<sub>3</sub>–B and Fe<sub>2</sub>O<sub>3</sub>–S–X. $^a$ 

Nanostructures	τ <sub>1</sub> (ps)	τ <sub>2</sub> (ps)	τ <sub>3</sub> (ns)	<i>I</i> <sub>1</sub> (%)	<i>I</i> <sub>2</sub> (%)	I <sub>3</sub> (%)
Fe <sub>2</sub> O <sub>3</sub> -B	182.2	390.7	2.052	71.7	27.2	1.13
$Fe_2O_3-S-20$	183.6	412.2	2.182	67.1	30.6	2.21
Fe <sub>2</sub> O <sub>3</sub> -S-50	183.2	420.3	3.09	54.0	42.2	3.81
Fe <sub>2</sub> O <sub>3</sub> -S-80	181.7	425.3	3.71	41.9	57.0	2.08
Fe <sub>2</sub> O <sub>3</sub> -S-110	184.1	417.5	7.115	53.4	45.1	1.48

 $a_{\tau}$ : positron lifetime components of different types of defects. *I*: relative intensity of different types of defects.

**Table 2** Theoretically calculated positron lifetime ( $\tau$ ) values of different types of defects in  $\alpha$ –Fe<sub>2</sub>O<sub>3</sub>.

Defect type	free	$V_{\scriptscriptstyle m O}^{{\scriptscriptstyleullet}{\scriptscriptstyleullet}}$	$V_{ ext{Fe}}^{"}$
τ (ps)	145	158	179

 $<sup>\</sup>overline{{}^a\tau}$ : positron lifetime components of different types of defects.

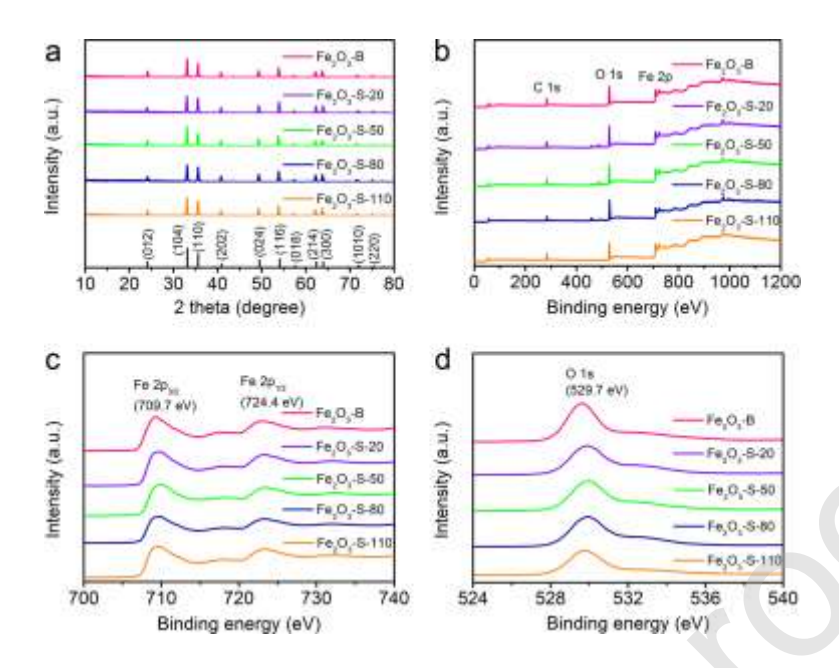


**Fig. 1.** XRD patterns (a), XPS full survey spectra (b), Fe 2p XPS spectra (c) and O 1s XPS spectra (d) of the Fe<sub>2</sub>O<sub>3</sub>–B and Fe<sub>2</sub>O<sub>3</sub>–S–X.

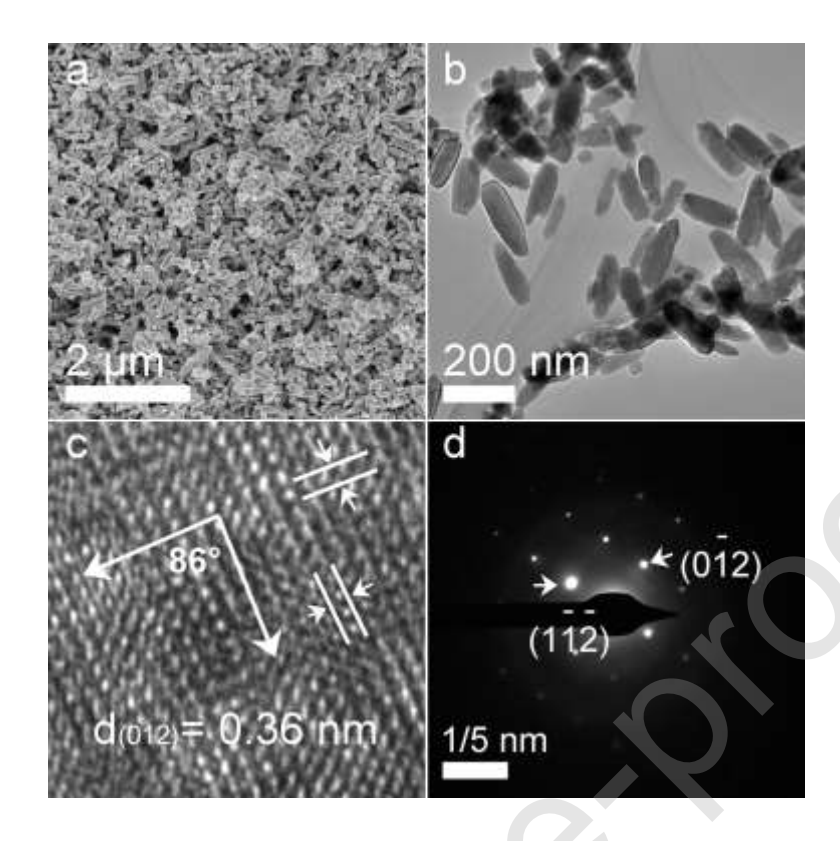


**Fig. 2.** SEM image (a); typical TEM image (b); HR-TEM image (c); and SAED pattern (d) of Fe<sub>2</sub>O<sub>3</sub>-S-80.

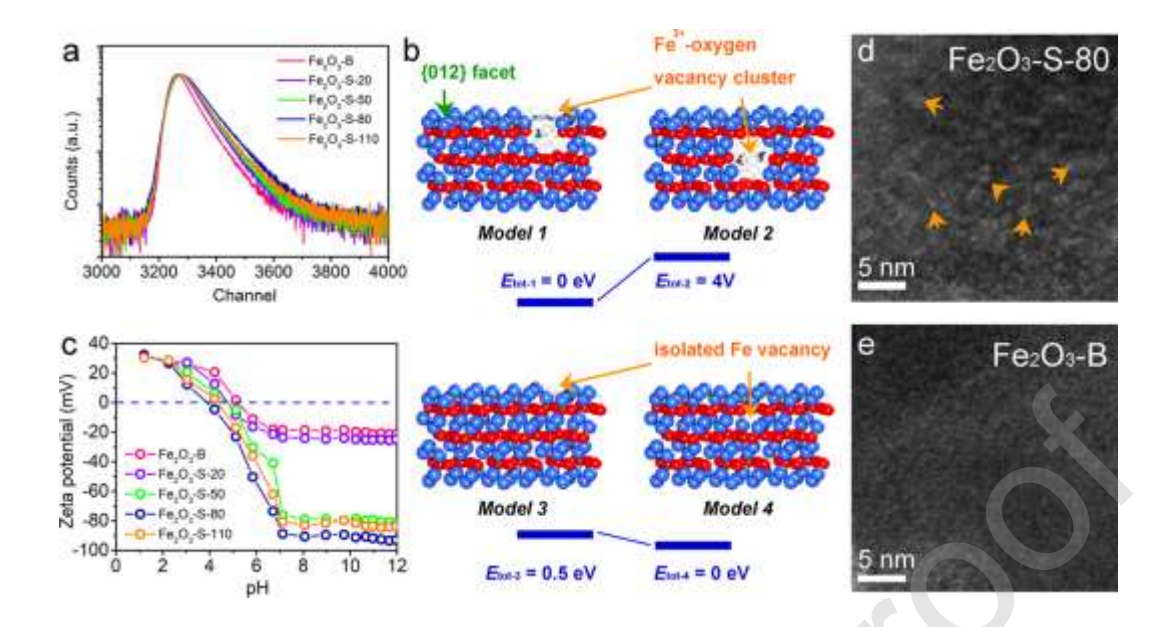


**Fig. 3.** Positron annihilation spectra of Fe<sub>2</sub>O<sub>3</sub>–B and Fe<sub>2</sub>O<sub>3</sub>–S–X (a); schematic representations of the four models, blue and red spheres depict Fe and O atoms, respectively (b); zeta–potentials patterns of Fe<sub>2</sub>O<sub>3</sub>–B and Fe<sub>2</sub>O<sub>3</sub>–S–X (c); HR–TEM images of Fe<sub>2</sub>O<sub>3</sub>–S–80 (d) and Fe<sub>2</sub>O<sub>3</sub>–B (e).

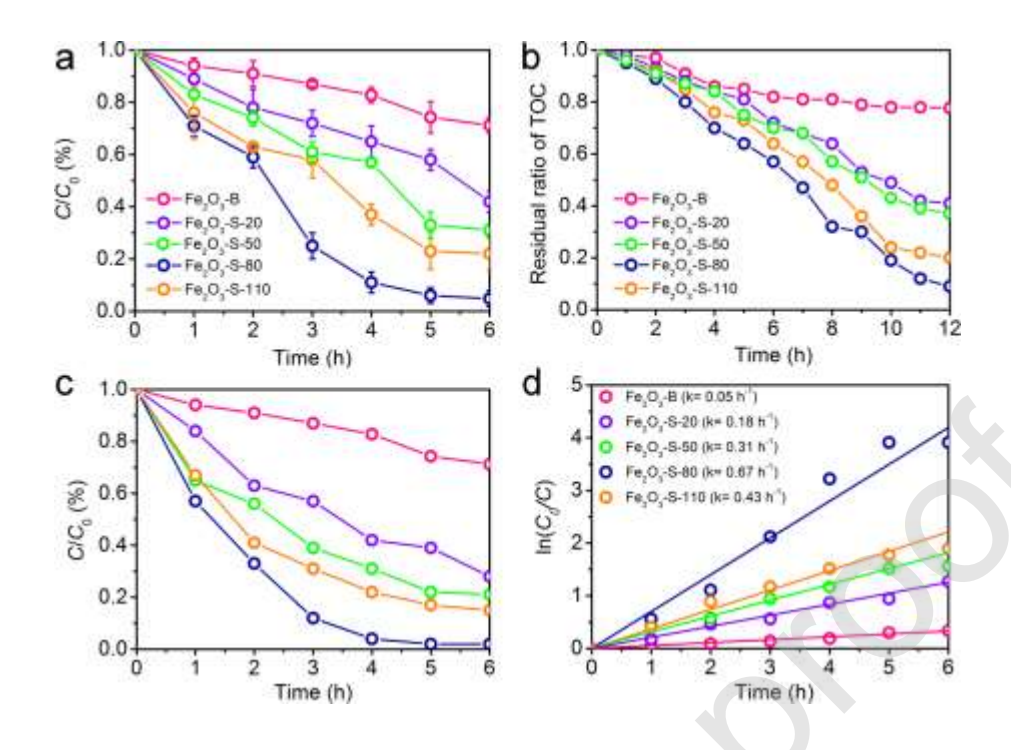


**Fig. 4.** Photodegradation of BPA with different photocatalysts (at same concentration, 1 gL<sup>-1</sup>) under visible light irradiation (a) and reduction of TOC (b). Photodegradation of BPA with different photocatalysts (at same surface area, the concentration of Fe<sub>2</sub>O<sub>3</sub>–B was 1 gL<sup>-1</sup>, Fe<sub>2</sub>O<sub>3</sub>–S–20 was 1.64 gL<sup>-1</sup>, Fe<sub>2</sub>O<sub>3</sub>–S–50 was 1.48 gL<sup>-1</sup>, Fe<sub>2</sub>O<sub>3</sub>–S–80 was 1.32 gL<sup>-1</sup> and Fe<sub>2</sub>O<sub>3</sub>–S–110 was 1.30 gL<sup>-1</sup>,) under visible light irradiation (c) and corresponding selected fitting results using pseudo-first-order reaction kinetics (d). The initial concentration of BPA was 10<sup>-5</sup> M. Error bars represent ± one standard deviation from the mean (n= 3).

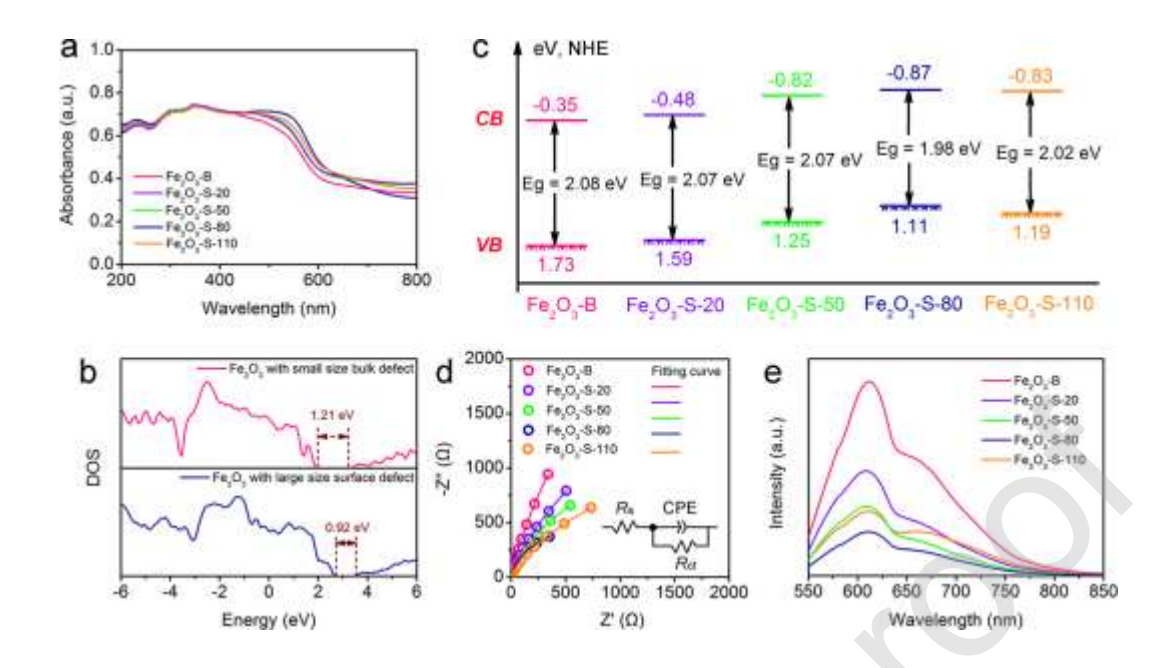


**Fig. 5.** The UV-vis spectra (a); density of states (DOS), the Fermi level is set to 0 eV (b); band gap structures (c); EIS Nyquist plots (d) and PL spectra (e) for Fe<sub>2</sub>O<sub>3</sub>-B and Fe<sub>2</sub>O<sub>3</sub>-S-X.

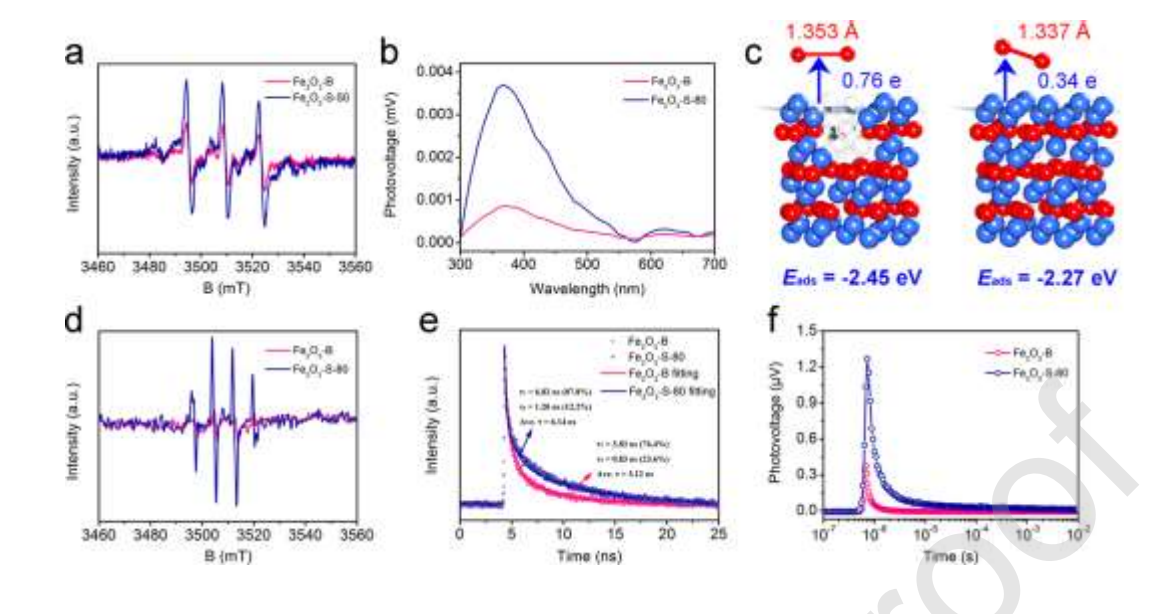


**Fig. 6.** DMPO ESR spectra under visible-light for 15 min in a methanol dispersion for O2<sup>--</sup> (a); SS-SPV spectra (b) of Fe<sub>2</sub>O<sub>3</sub>−B and Fe<sub>2</sub>O<sub>3</sub>−S−80; calculated O<sub>2</sub> adsorption energy (*E*<sub>ads</sub>, negative means heat release), bader effective charge for the carried electrons of O<sub>2</sub> molecules (Negative means electrons accumulation and positive means electrons depletion), O−O bond length of O<sub>2</sub> molecule adsorbed on Model 1 (left) and Model 4 (right), blue and red spheres depict Fe and O atoms, respectively (c); DMPO ESR spectra under visible-light for 15 min in an aqueous dispersion for •OH (d); time-resolved PL spectra (e) and TS-SPV spectra (f) of Fe<sub>2</sub>O<sub>3</sub>−B and Fe<sub>2</sub>O<sub>3</sub>−S−80.

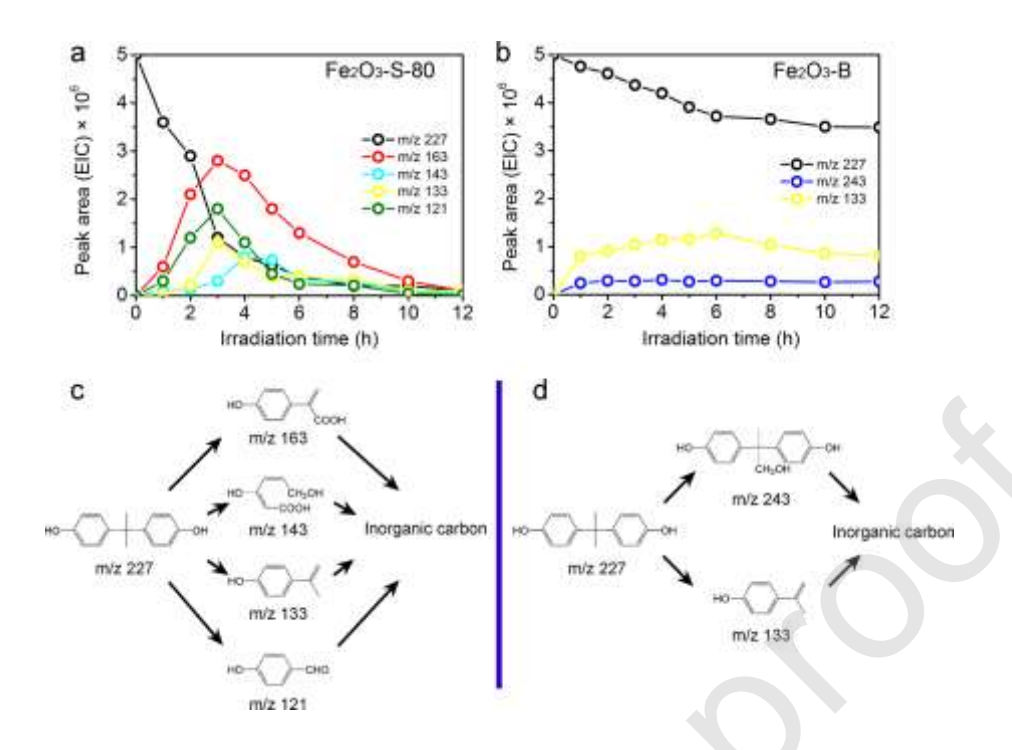


**Fig. 7.** Degradation of bisphenol A (BPA) and evolution of product ions during photodegradation experiment in the presence of Fe<sub>2</sub>O<sub>3</sub>–S–80 (a) and Fe<sub>2</sub>O<sub>3</sub>–B (b); proposed reaction pathways of BPA photodegradation in the presence of Fe<sub>2</sub>O<sub>3</sub>–S–80 (c) and Fe<sub>2</sub>O<sub>3</sub>–B (d).